ARMA 16-107

Damage and healing model of stiffness and permeability for salt rock: microstructure imaging, fabric processes and continuum mechanics

Zhu, C. and Arson, C.

School of Civil and Environmental Engineering, Georgia Institute of Technology, Atlanta, Georgia

This paper was prepared for presentation at the 50th US Rock Mechanics / Geomechanics Symposium held in Houston, Texas, USA, 26-29 June 2016. This paper was selected for presentation at the symposium by an ARMA Technical Program Committee based on a technical and critical review of the paper by a minimum of two technical reviewers. The material, as presented, does not necessarily reflect any position of ARMA, its officers, or members. Electronic reproduction, distribution, or storage of any part of this paper for commercial purposes without the written consent of ARMA is prohibited. Permission to reproduce in print is restricted to an abstract of not more than 200 words; illustrations may not be copied. The abstract must contain conspicuous acknowledgement of where and by whom the paper was presented.

ABSTRACT: In this study, we proposed a fabric-enriched Continuum Damage Mechanics model to investigate the coupled influence of damage and healing on the mechanical and transport properties of salt rock. In order to infer the form of fabric tensors, we carried out creep tests on granular salt assemblies under constant temperature and humidity conditions and used micro-computed tomography for microstructure characterization. Using microscope imaging and micro-CT scanning, we analyzed the probability distributions of crack radius, void areas and crack spacing and used them as a basis to derive macroscopic evolution laws. A stress path comprising a tensile loading, a compressive unloading, a creep-healing stage, and a reloading was simulated. As expected, stiffness decreases (respectively increases) and permeability increases (respectively decreases) upon damage (respectively healing). Results also highlight the increased efficiency of healing with temperature. The micro-macro relationships established by statistical image analysis also provide the evolution of microstructure descriptors during the test. Simulations show that permeability changes are controlled by changes in crack connectivity, which dominate changes of porosity. The proposed framework is expected to improve the fundamental understanding of coupled processes that govern microstructure changes and subsequent variations of stiffness and permeability in salt rock, which will allow the assessment of the long-term performance of geological storage facilities.

1. INTRODUCTION

The very low permeability of salt rock is its principal advantage for nuclear waste disposals and high-pressure gas storage. During secondary creep, dislocation glide produces isochoric deformation. Geometric incompatibilities between grains result in grain pile-ups, stress concentrations, and crack propagation. The coalescence of cracks can increase permeability by several orders of magnitude, which is very critical to the long-term performance of geological storage facilities in salt.

Many approaches have been proposed to predict the permeability in rocks. A large number of models are based on Kozeny-Carman relationship to link permeability with porosity. However, experimental results indicate that when micro-cracks propagate in salt, permeability increases significantly, whereas the change in porosity is moderate (e.g., Gloyna and Reynolds, 1961; Peach, 1990). Guéguen and Dienes (1989) first introduced the percolation concept and proposed pipe and crack models to estimate permeability in rock materials. A geometrical model based on the Bethe Lattice was then proposed to improve this crack model (Peach and Spiers, 1996). Oda et al. (2002) used a fabric tensor to deduce the variations of the anisotropic permeability tensor during damage propagation in granite. Researchers have also made efforts in incorporating microstructure parameters such as the tortuosity and the specific pore surface area into the classical Kozeny-Carman model (e.g., Chan et al., 2001). However, most of these frameworks do not take into account the evolution of mechanical properties, especially under the coupled influence of damage and healing.

Thermo-mechanical models of damage and healing proposed in continuum mechanics for salt resort to the concept of dilatancy boundary (Hou, 2003). Anisotropic healing models based on Continuum Damage Mechanics (CDM) usually depend on the concept of "net damage", which allows modeling stiffness degradation (damage) and recovery (healing). These theoretical frameworks are purely hypothetical and do not allow the prediction of all coupled processes that occur in actual rock materials. Damage models that distinguish crack closure and rebonding in rocks conveniently model all dissipation processes with rate-dependent evolution laws, which avoids implementing threshold-based yield functions in numerical codes. Unfortunately, those models do not properly represent the brittle behavior resulting from rate-independent crack opening and closure. In such models, healing is defined as a particular form of crack

closure detected by an increment in wave velocity, rather than crack rebonding.

The ultimate goal of this research work is to understand the fundamental microscopic mechanisms that cause stiffness and permeability evolution in salt rock during damage and healing processes. We use the thermo-mechanical model that we proposed in (Zhu and Arson, 2015a) as basis to predict the effect of crack opening, closure, and healing on the mechanical and transport properties. We explain the choice of fabric descriptors in Section 2. The multi-scale theoretical framework coupling damage and healing is presented in Section 3. In Section 4, we explain the upscaling method and the computation algorithm. Simulation results from a loading-unloading stress path are presented in Section 5 to show the influence of damage and healing on the coupled evolution of microstructure, stiffness, and permeability.

2. FABRIC CHARACTERIZATION

Fabric evolution during damage and healing processes determines the mechanical and transport properties of salt rock. Nondestructive observation of fabric evolution under complex variations of stress, temperature, and moisture remains an experimental challenge. We carried out creep tests on table salt by confining those particles in tubes and loading them axially by a spring (Fig. 1a). We used an environmental chamber to maintain a constant humidity environment (relative humidity = 75%) at room temperature (22^{o}C). Table salt is a granular assembly that has the same crystallographic structure as salt rock. We used it as an analog of salt rock in this experimental study, because no large equipment is needed to apply creep loads required to study creep processes (as opposed to solid rock). Therefore in the following, open contacts at grain faces are considered as micro-cracks in the damage model.

In our previous works, we did microscope observations of the salt assembly through the tube walls at regular time intervals in order ensure continuous microstructure characterization without taking out the sample (Zhu and Arson, 2015a). However, light reflection and transmission induced by transparent and cubic-shaped grains significantly impaired the image quality, which increased the difficulty to detect grain boundaries. To overcome this problem, we use micro-computed tomography (micro-CT) to observe and re-generate the 3D porous structure of the granular salt assembly. This technique can easily be used to distinguish the solid NaCl from voids, which have a strong density contrast. Micro-CT observations were conducted at the Guldberg Laboratory at Georgia Tech. The voxel size was 30μm while the size of a single particle is $300\sim400\mu m$. We used *ImageJ* (Abramoff et al., 2004) for 3D solid skeleton reconstruction (Fig. 1b). Cross-sectional views were produced throughout the sample (Fig. 1c), from which we extracted binary images with further image processing (Fig. 1d).

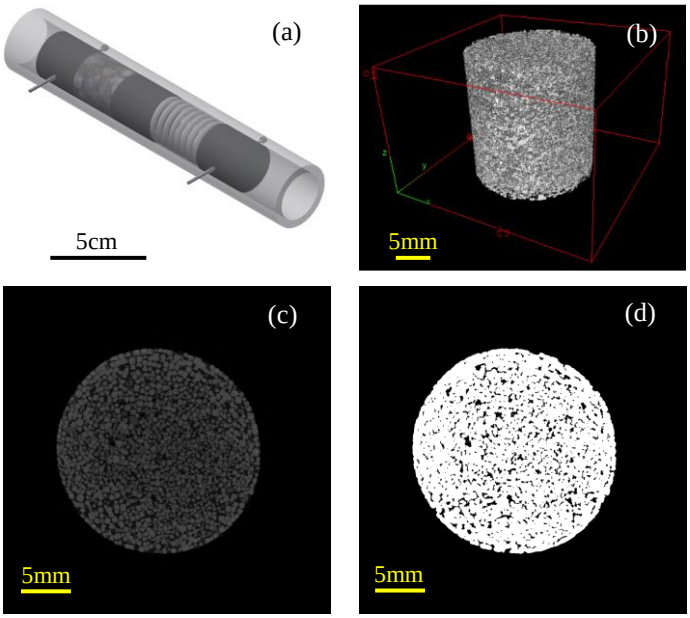

Fig. 1. Image analysis during creep tests realized on table salt: (a) experimental set up; (b) micro-CT image of the solid skeleton; (c) cross-sectional view (original image); (d) cross-sectional view (binary image). Voxel size = 30μm. Sample diameter = 19mm. Grain size = 300~400μm.

We performed statistical image analyses of the binary images to extract information on the fabric. In particular, we characterized pore connectivity by the studying the distribution of void centroid-to-centroid distances. Using the location of the void centroids (Fig. 2), we calculated the distance between this centroid and the centroid of the nearest void. We found that these relative distances follow a lognormal distribution (Fig. 3):

$$p_i(l_i) = \frac{1}{\sqrt{2\pi} l_i s_i} e^{-\frac{(\ln l_i - m_i)^2}{2 s_i^2}} \quad (1)$$

This lognormal distribution reaches its peak value at a distance of about 0.4 mm, which correponds to the typical size of a table salt grain.

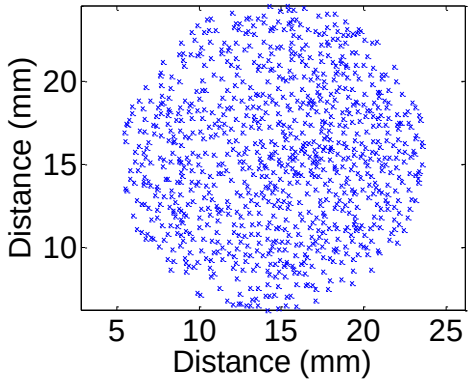

Fig. 2. Locations of void centroids processed from the binary image in Fig. 1d.

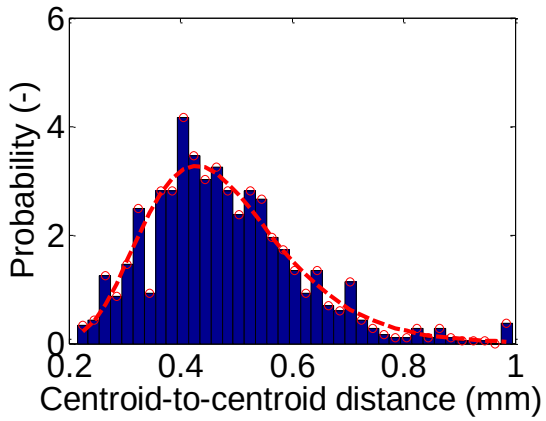

Fig. 3. Normalized probabilty distribution of the centroid-to-centroid distances for all voids in the binary image (Fig. 1d). The peak appears at about 0.4 mm, which is close to the typical size of a single table salt grain.

We also analyzed the distribution of void surface areas, which was found to follow a power law distribution (Fig. 4), which is conform to our previous observations (Zhu and Arson, 2015a):

$$p_A(A_v) = a \cdot A_v^t \quad (2)$$

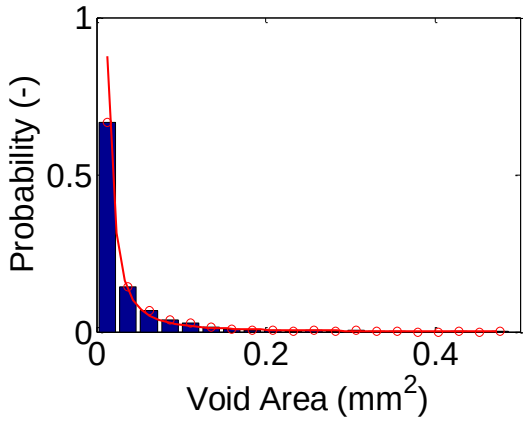

Fig. 4. Normalized power law distribution of void area processed from the binary image in Fig. 1d.

For future study, with these fabric characteristics, we will develop a pore network model to account for flow anisotropy. Image analysis in 3D is also necessary to more accurately represent the features of the fabric.

3. THEORETICAL FRAMEWORK

Based on the theoretical framework developed in (Zhu and Arson, 2014), we propose a Continuum Damage Mechanics (CDM) model to couple microscopic and macroscopic thermo-mechanical evolution laws (Table 1). This CDM model captures the influence of damage and healing on the mechanical and transport properties of salt rock.

3.1. Continuum Damage Model

For a typical loading-unloading stress path, total strain can be decomposed into three components (Fig. 5). The purely elastic strain $\boldsymbol{\varepsilon^{el}}$ is recoverable upon unloading. The damage-induced strain $\boldsymbol{\varepsilon^{d}}$ has two components: $\boldsymbol{\varepsilon^{ed}}$ is the damage-induced elastic deformation, $\boldsymbol{\varepsilon^{id}}$ is the irreversible deformation due to residual crack openings. The summation of $\boldsymbol{\varepsilon^{el}}$ and $\boldsymbol{\varepsilon^{ed}}$ gives the total elastic deformation $\boldsymbol{\varepsilon^{E}}$ (Table 1). The additional compression stress required to compensate $\boldsymbol{\varepsilon^{id}}$ is referred to as the residual stress and is expressed as:

$$\boldsymbol{\sigma_R = -D(\Omega)}: \boldsymbol{\varepsilon^{id}} \quad (3)$$

In which $\boldsymbol{D}$ is the stiffness tensor, $\boldsymbol{D_0}$ is the stiffness in the undamaged state. $\boldsymbol{\Omega}$ is the second-order damage tensor.

As shown in Table 1, we decompose the solid skeleton free energy into the purely thermo-elastic deformation energy (ψ_s^{ET}) and the potential energy of crack faces ($\psi_s^{\Omega T}$). The expressions of stress and damage driving force are deduced from thermodynamic conjugation relaionships. Based on a dimensional analysis, we can show that the quadratic term in temperature $\frac{\tau^2}{2\tau_0}\frac{\partial C(\Omega)}{\partial \Omega}$ is negligible. For simplicity, we considered that the damage criterion is independent of temperature variation. The active damage driving force ($\boldsymbol{Y_d}$) is further simplified as a function of total strain only. We adopt an associative damage flow rule, with f_d used as the damage potential.

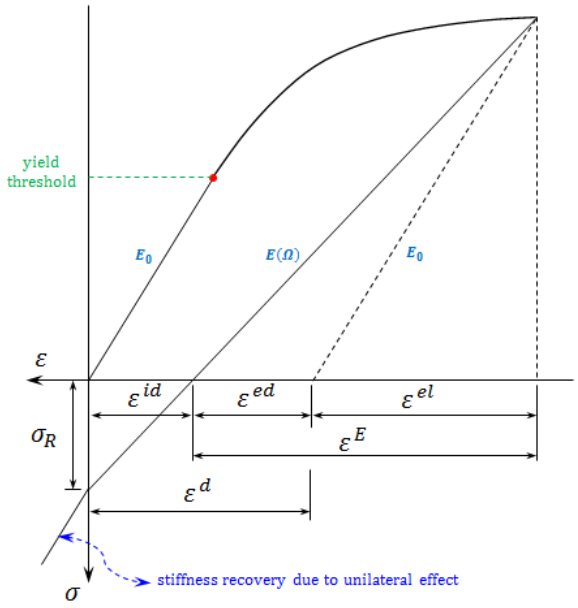

Fig. 5. Typical stress-strain curve showing the decomposition of total strain. Note that compression is counted positive.

To capture the hardening phenomenon, which accounts for the increase of energy needed for growth of micro-cracks as damage accumulates, the damage criterion is expressed in the form of a linear function of damage.

Table 1. Outline of thermo-mechanical damage and healing model

Postulates	
Free Energy for Crack Opening (Ψ_S)	$\psi_s = \psi_s^{ET} + \psi_s^{\Omega T} = \left[\frac{1}{2}\boldsymbol{\varepsilon}^{el}:\boldsymbol{D_0}:\boldsymbol{\varepsilon}^{el} - \frac{C_0\tau^2}{2\tau_0} - \tau\boldsymbol{K_0}:\boldsymbol{\varepsilon}^{el}\right] + [\frac{1}{2}\boldsymbol{\varepsilon}^{d}:\boldsymbol{D}(\boldsymbol{\Omega}):\boldsymbol{\varepsilon}^{d} - \frac{C(\boldsymbol{\Omega})\tau^2}{2\tau_0} - \tau\boldsymbol{K}(\boldsymbol{\Omega}):\boldsymbol{\varepsilon}^{d}]$ $\frac{1}{2}\boldsymbol{\varepsilon}^{d}:\boldsymbol{D}(\boldsymbol{\Omega}):\boldsymbol{\varepsilon}^{d} = \frac{1}{2}\lambda\left(tr\boldsymbol{\varepsilon}^{d}\right)^2 + \mu tr\left(\boldsymbol{\varepsilon}^{d}\cdot\boldsymbol{\varepsilon}^{d}\right) + \alpha tr\boldsymbol{\varepsilon}^{d} tr\left(\boldsymbol{\varepsilon}^{d}\cdot\boldsymbol{\Omega}\right) + 2\beta tr\left(\boldsymbol{\varepsilon}^{d}\cdot\boldsymbol{\varepsilon}^{d}\cdot\boldsymbol{\Omega}\right)$
Free Energy for Crack Closure (Ψ_S)	$\psi_s = \left[\frac{1}{2}\boldsymbol{\varepsilon}^{el}:\boldsymbol{D_0}:\boldsymbol{\varepsilon}^{el} - \frac{C_0\tau^2}{2\tau_0} - \tau\boldsymbol{K_0}:\boldsymbol{\varepsilon}^{el}\right] + [\frac{1}{2}\boldsymbol{\varepsilon}^{d}:\boldsymbol{D}^*(\boldsymbol{\Omega}):\boldsymbol{\varepsilon}^{d} - \frac{C^*(\boldsymbol{\Omega})\tau^2}{2\tau_0} - \tau\boldsymbol{K}^*(\boldsymbol{\Omega}):\boldsymbol{\varepsilon}^{d}]$ For $0 < \eta \leq 1$, $\boldsymbol{D}^*(\boldsymbol{\Omega}) = \boldsymbol{D}(\boldsymbol{\Omega}) + \eta\sum_{i=1}^{3} H\left(-tr(\boldsymbol{P}_i:\boldsymbol{\varepsilon})\right)\boldsymbol{P}_i:\left(\boldsymbol{D_0} - \boldsymbol{D}(\boldsymbol{\Omega})\right):\boldsymbol{P}_i;$ $\boldsymbol{K}^*(\boldsymbol{\Omega}) = \boldsymbol{K}(\boldsymbol{\Omega}) + \eta\sum_{i=1}^{3} H\left(-tr(\boldsymbol{P}_i:\boldsymbol{\varepsilon})\right)\boldsymbol{P}_i:\left(\boldsymbol{K_0} - \boldsymbol{K}(\boldsymbol{\Omega})\right):\boldsymbol{P}_i;$ $C^*(\boldsymbol{\Omega}) = C(\boldsymbol{\Omega}) + \eta\sum_{i=1}^{3} H\left(-tr(\boldsymbol{P}_i:\boldsymbol{\varepsilon})\right)\boldsymbol{P}_i:\left[\left(C_0 - C(\boldsymbol{\Omega})\right)\boldsymbol{\delta}\otimes\boldsymbol{\delta}\right]:\boldsymbol{P}_i$
Free Energy for Crack Rebonding (Ψ_S)	Replace $\boldsymbol{\Omega}$ by $\boldsymbol{A}$ in the free energy for crack closure $\boldsymbol{A} = \boldsymbol{\Omega} - \boldsymbol{\delta}h$
Damage Criterion (f_d)	$f_d(\boldsymbol{Y_d}, \boldsymbol{\Omega}) = \sqrt{\frac{1}{2}\boldsymbol{Y_d}:\boldsymbol{Y_d}} - [a_0 + a_1 tr(\boldsymbol{\Omega})]$
Strain Decomposition	$\boldsymbol{\varepsilon} = \boldsymbol{\varepsilon}^{\boldsymbol{E}} + \boldsymbol{\varepsilon}^{\boldsymbol{id}} = \boldsymbol{\varepsilon}^{\boldsymbol{el}} + \boldsymbol{\varepsilon}^{\boldsymbol{d}} = \boldsymbol{\varepsilon}^{\boldsymbol{el}} + \boldsymbol{\varepsilon}^{\boldsymbol{ed}} + \boldsymbol{\varepsilon}^{\boldsymbol{id}}$
Diffusion Equation	$\bar{u}(t) = < u(x,t) > = \frac{1}{l}\int_0^l u(x,t)dx = \frac{8U_0}{\pi l}\sum_{i=1,3,5,\dots}^{\infty}\frac{e^{-\lambda_n^2 D_c t}}{n\lambda_n}$ $D_c = D_{c0}e^{-\frac{Q}{RT}}$ $h(t) = 1 - \bar{u}(t)$
Conjugation relationships	
Stress ($\boldsymbol{\sigma}$)	$\boldsymbol{\sigma} = \frac{\partial\psi_S}{\partial\boldsymbol{\varepsilon}^{el}} = \boldsymbol{D_0}:\boldsymbol{\varepsilon}^{el} - \tau\boldsymbol{K_0}$
Damage Driving Force (Y_d)	$\boldsymbol{Y} = -\frac{\partial\psi_S}{\partial\boldsymbol{\Omega}} = -\left[\boldsymbol{D}(\boldsymbol{\Omega}):\boldsymbol{\varepsilon}^{d}\right]:\frac{\partial\boldsymbol{\varepsilon}^{d}}{\partial\boldsymbol{\Omega}} - \frac{1}{2}\boldsymbol{\varepsilon}^{d}:\frac{\partial\boldsymbol{D}(\boldsymbol{\Omega})}{\partial\boldsymbol{\Omega}}:\boldsymbol{\varepsilon}^{d} + \frac{\tau^2}{2\tau_0}\frac{\partial C(\boldsymbol{\Omega})}{\partial\boldsymbol{\Omega}} + \tau\boldsymbol{K}(\boldsymbol{\Omega}):\frac{\partial\boldsymbol{\varepsilon}^{d}}{\partial\boldsymbol{\Omega}} + \tau\frac{\partial\boldsymbol{K}(\boldsymbol{\Omega})}{\partial\boldsymbol{\Omega}}:\boldsymbol{\varepsilon}^{d}$ $\boldsymbol{Y_d} = -(\alpha + 2\beta)\boldsymbol{\varepsilon}\cdot\boldsymbol{\varepsilon}$

α, β	=	mechanical damage parameters (Pa)	a_0	=	initial damage threshold (Pa)
λ, μ	=	Lam$\acute{e}$ coefficients (Pa)	a_1	=	damage hardening parameter (Pa)
τ_0	=	initial temperature (K)	g	=	toughness parameter (Pa)
$\boldsymbol{D}$	=	damaged stiffness tensor (Pa)	k	=	bulk modulus (Pa)
α_T	=	thermal expansion coefficient (K^{-1})	$\boldsymbol{K}$	=	$k\alpha_T$ "diagonal tensor" (-)
$\boldsymbol{D}^*$	=	effective stiffness tensor after "partial recovery" (Pa)	C	=	damaged heat capacity (J/K)
$\boldsymbol{K}^*$	=	effective diagonal tensor after "partial recovery" (Pa)	A	=	TM damage parameter (-)
C^*	=	effective heat capacity after "partial recovery" (J/K)	η	=	degree of maximum stiffness recovery (-)
$\boldsymbol{P}_i$	=	4th order project tensor for the projection in crack planes normal to direction i (-)	$\boldsymbol{\delta}$	=	second order identity tensor (-)

We adopt Chaboche's (1992) approach to account for the effect of crack closure. Rock stiffness depends on a Heaviside function to distinguish the behaviors in tension and compression. The number of inter-granular contacts in the Representative Element Volume (REV) increases after crack closure, which results in a recovery of stiffness ($\boldsymbol{D}^*(\boldsymbol{\Omega})$) as well as heat capacity ($C^*(\boldsymbol{\Omega})$). A coefficient (η in Table 1) controls the influence of these unilateral effects of crack closure on stiffness and strength variations.

3.2. Diffusion-controlled healing model

A distinction is made between crack closure and crack healing. Crack healing occurs only if sufficient energy input is provided to trigger the migration of ions within the lattice. In our model, we assume that the main driving factor for crack rebonding is diffusive mass transfer (DMT). Cracks (i.e., grain-to-grain contact openings in our experiment) tend to be rebonded by different ionic species at the crack faces. During DMT healing, crack rebonding starts at the periphery of the cracks and proceeds towards the center. Note that DMT is only one of many possible phenomena that explain healing in salt. In a companion paper, we characterize the transition between diffusion-dominated kinetics and dissolution-precipitation dominated kinetics for salt healing governed by pressure solution (Shen et al., under review).

Because of the uniform distribution of grain orientations, intra-granular diffusion is assumed to be isotropic, which reduces the healing tensor H into a scalar h: $\boldsymbol{H} = h\boldsymbol{\delta}$. Damage is a rate-independent dissipation variable in this model and cannot decrease – in virtue of the consistency equation. We introduce a mixed damage variable $\boldsymbol{A}$ to account for the effect of healing on stiffness and permeability. Therefore in the coupled damage and healing model adopted in the following, the damage variable $\boldsymbol{\Omega}$ is replaced by the net damage variable $\boldsymbol{A}$ in the expressions of the recovered stiffness and heat capacity.

We use a diffusion equation to model the migration of sodium ions from the salt grain bulk to its boundaries. The intensity of net damage, defined as $u = U_0 - h$, satisfies the following diffusion equation:

$$\frac{\partial u}{\partial t} = D_c \nabla^2 u \tag{4}$$

in which D_c is the diffusion coefficient. We take half of the edge length of the grain as the maximum diffusion distance. During healing, ions migrate to a crack face and electronic forces bond these ions to the lattice of the opposite crack face. At the grain periphery, the net damage is taken as zero (i.e. rebonding starts at the periphery of the grains and progresses towards the center). The initial conditions considered in the diffusion problem are therefore:

$$h(x, t=0) = 0, \quad u(x, t=0) = U_0 \tag{5}$$

Hence, the solution writes:

$$u(x,t) = \frac{4U_0}{\pi} \sum_{i=1,3,5,\ldots}^{\infty} \frac{e^{-\lambda_n^2 D_c t} \sin(\lambda_n x)}{n} \tag{6}$$

In which $\lambda_n = \frac{n\pi}{l}$. The space average of the density of net damage ($\bar{u}(t)$) is provided in Table 1. The diffusion coefficient D_c depends on both pressure and temperature. More activation energy is required for a chloride ion to jump into a chloride vacancy than for a sodium ion to jump into a sodium ion vacancy (Mapother et al., 1950). So we assume that migration of sodium ion dominates the diffusion of sodium chloride. Within the temperature range of 573K~973K, Mapother et al. (1950) found a logarithmic relationship between the diffusion coefficient and temperature:

$$D_c = -\frac{1.67 \times 10^{-12}}{T} + 2.99 \times 10^{-15} \tag{7}$$

in which T is expressed in Kelvin, D_c is in m^2/s.

3.3. *Fabric-based permeability model*

Fabric evolution impacts both the mechanical stiffness and the hydraulic properties of salt rock. In our theoretical model of salt rock, we considered that cracks (i.e. grain contact openings in the experiment performed on table salt) were 3D spheroids (Fig. 6a). Compared to penny-shaped cracks, spheroidal cracks have a more realistic shape and can be easily described by a similar set of microstructural descriptors: radius R, aperture 2λ, and orientation n. L is the crack spacing, i.e., the centroid-to-centroid distance between adjacent cracks (Fig. 6b).

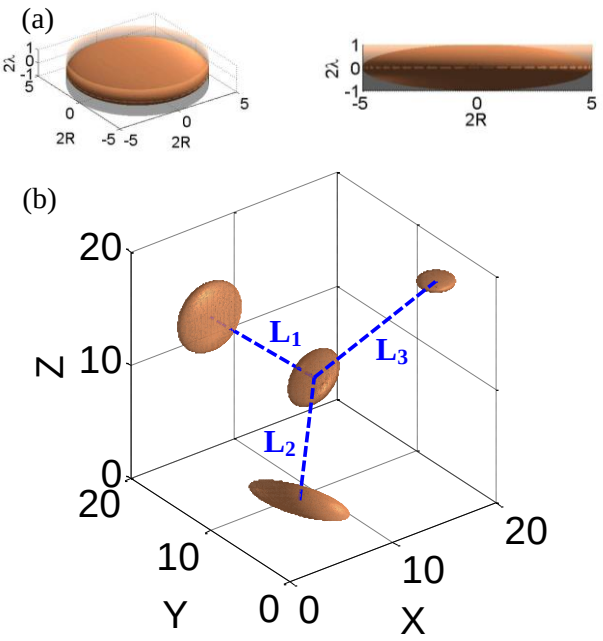

Fig. 6. (a) Comparison between a spheroidal crack and a penny-shaped crack (3D view and 2D view). (b) Characterization of the spatial distribution of spheroidal cracks. Each crack is characterized by its radius, aperture, orientation, and the crack spacing.

We use the crack model proposed by Dienes (1982) and further modified by Guéguen and Dienes (1989) as a basis to calculate permeability. For an isotropic distribution of cracks with narrowly distributed width, radius, and spacing, the permeability can be computed as:

$$k = \frac{4\pi}{15} f \frac{\bar{\lambda}^3 \bar{R}^2}{\bar{l}^3} \tag{8}$$

in which $\bar{\lambda}$ is the average half-crack aperture, $\bar{R}$ is the average crack radius, $\bar{l}$ is the average crack spacing, and the connectivity factor f accounts for the fraction of cracks that belong to an infinite network (i.e., the fraction of cracks that passed the percolation threshold). These three microstructural parameters are independent from each other. From the CT-scan image analysis presented in Section 2 and from our previous microscope observations (Zhu and Arson, 2015a), we know the probability density functions of these fabric descriptors: the crack radius follows a lognormal distribution; the crack area follows a power law distribution (Fig. 4); the

crack spacing follows a lognormal distribution (Fig. 3). f is determined by the percolation theory.

In this model, spheroidal cracks are allowed to grow, intersect, and form permeable pathways. Such pathways are limited to local regions at low crack number densities, but percolation can occur after a critical density is reached. Percolation originates macroscopic permeability. After the percolation threshold is reached, permeability rapidly increases with crack density. Crack spacing is set as a constant in this model, i.e. crack centroids are assumed to remain the same upon crack growth (this means that cracks grow symmetrically about their centroid). In the absence of further experimental evidence, this assumption was considered acceptable for the proposed model of permeability.

The projection of orderly-packed granular salt assembly in 2D shows that each void has a maximum number of four neighboring voids. Therefore, we used the four-fold coordinated Bethe lattice (Stauffer, 1985) adopted by Dienes (1982) to calculate f. In a future study, we will resort to a pore network model to predict the value of f. For the chosen Bethe lattice, the percolation probability, which is used to determine whether a crack is connected to at least two infinite paths for throughout flow, is given by:

$$f = 1 - 4\left[\sqrt{\frac{1}{p} - \frac{3}{4}} - \frac{1}{2}\right]^3 + 3\left[\sqrt{\frac{1}{p} - \frac{3}{4}} - \frac{1}{2}\right]^4 \quad (9)$$

in which p is the probability of existence of a bond, which is equivalent to the probability of intersection between two cracks in our model. We adopt the concept of excluded volume (De Gennes, 1976) to calculate p. The excluded volume is the average volume around one crack within which a second crack must have its center in order for the cracks to intersect. For two discs, the excluded volume is found as:

$$V_e = \pi^2 \bar{R}^3 \quad (10)$$

Given that $1/\bar{l}^3$ is the crack density, the probability of crack intersection is given as (Guéguen and Dienes, 1989):

$$p \approx \frac{\pi^2 \bar{R}^3}{4\bar{l}^3} \quad (11)$$

in which it is assumed that each crack has 4 neighbors.

Combining Eqs (8), (9), and (11), the expression of permeability in terms of crack geometry and percolation parameters becomes:

$$f = \frac{4\pi}{15}\frac{\bar{\lambda}^3 \bar{R}^2}{\bar{l}^3}\left\{1 - 4\left[\sqrt{\frac{4\bar{l}^3}{\pi^2 \bar{R}^3} - \frac{3}{4}} - \frac{1}{2}\right]^3 + 3\left[\sqrt{\frac{4\bar{l}^3}{\pi^2 \bar{R}^3} - \frac{3}{4}} - \frac{1}{2}\right]^4\right\} \quad (12)$$

The value of k_{max} is given by Eq. (8) for $f = 1$. Nonzero permeability is observed for $p > \frac{1}{3}$: After this threshold is reached, the resulting crack intersection network will percolate and carry flows through the cluster of intersecting cracks (Fig. 7).

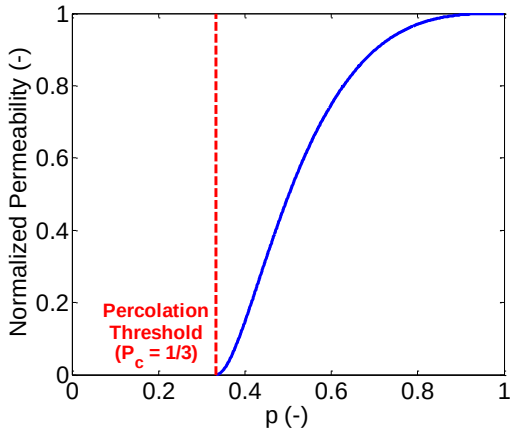

Fig. 7. The normalized permeability as a function of the probability of intersection between two cracks, p. The percolation threshold for the four-fold coordinated Bethe lattice is 1/3.

Two possibilities exist for the development of permeability from critical region ($f < 1$) to post-critical region ($f = 1$): (1) the crack number density increases without changing the average crack geometry after $f = 1$; (2) a constant population of cracks widen after $f = 1$. In this study, we fixed the total number of cracks and the crack spacing parameter, but crack geometry evolves during the damage and healing processes. For consistency, we thus used the 2nd scenario (crack widening) to model the increase of crack-permeability after percolation. Beyond the critical region, permeability is maximum:

$$k = \frac{4\pi}{15}\frac{\bar{\lambda}^3 \bar{R}^2}{\bar{l}^3} \quad (13)$$

3.4. Micro-Macro Relationships

Following the same methodology as in (Zhu and Arson, 2015a), we establish mathematical relationships (summarized in Table 2) between microstructure descriptors (crack radius, void area, crack spacing) and phenomenological variables of damage and healing. As illustrated in Fig. 8, projections of spheroidal cracks in the plane of observation (microscope images or CT-scan cross sectional views) are ellipses. Solid lines represent the shapes of the original cracks, while the dashed lines represent the deformed shapes. Note that in this

framework, the crack radius evolves during non-elastic processes only (damage propagation), whereas crack aperture changes during both elastic and non-elastic deformation.

Assuming that the principal directions of stress and net damage are parallel, we relate net damage eigenvalues ($\boldsymbol{A}$) to the means of the crack length components (η_j). In the probability density functions, we update only the means m_i and use a constant value for the standard deviations, which are insensitive to the variations of pressure and temperature conditions (Zhu and Arson, 2015a). As a result, the probability density function of R_j can be updated from the macroscopic strain as follows:

$$\Delta\varepsilon \overset{\text{Table 1}}{\rightarrow} \Delta\boldsymbol{A} \overset{\text{Table 2}}{\rightarrow} \boldsymbol{R} \overset{\text{Table 2}}{\rightarrow} p_j(R_j) \tag{14}$$

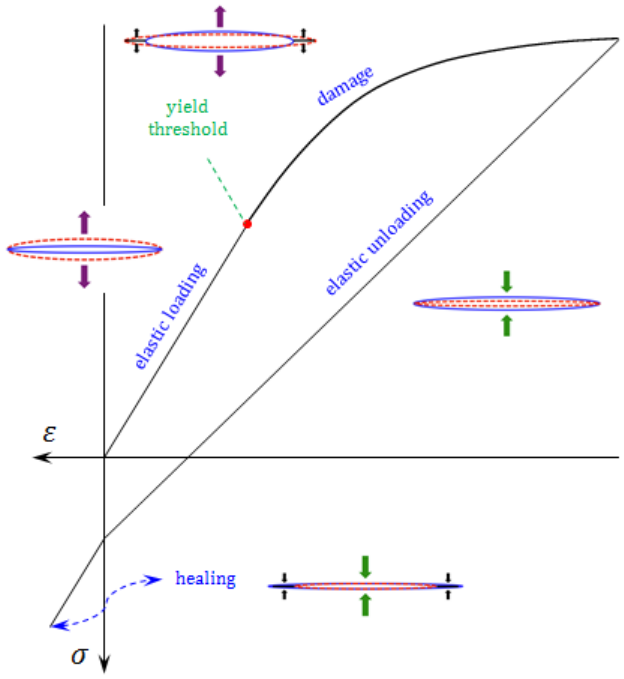

Fig. 8. Model of micro-crack geometric evolution during a loading-unloading cycle.

Grains are considered incompressible, therefore a porosity change in the REV is equal to REV volume change. We adopt the developed linear interpolation in (Zhu and Arson, 2015a) to link 2D porosity and 3D porosity. Given the range of possible values for porosity, we are able to update the probability density function of the void area as follows:

$$\Delta\varepsilon \rightarrow \Delta n_{3D} \overset{\text{Table 2}}{\rightarrow} \Delta n_{2D} \overset{\text{Table 2}}{\rightarrow} p_A(A_v) \tag{15}$$

In the future, we will directly retrieve such information from 3D porous structure images acquired with the micro-CT scan.

We apply the theory of fracture mechanics to compute the micro-crack opening vector of an ellipsoidal micro-crack propagating in mode I (Anderson, 2005). Therefore, the micro-crack displacement, equal to the half aperture, is a function of stress intensity, which further results in the relation between residual stress and crack aperture.

4. COMPUTATIONAL ALGORITHM

The full resolution algorithm is summarized in Fig. 9. In the simulations presented in the following, the computation is strain-controlled with a strain increment given at the beginning of each step.

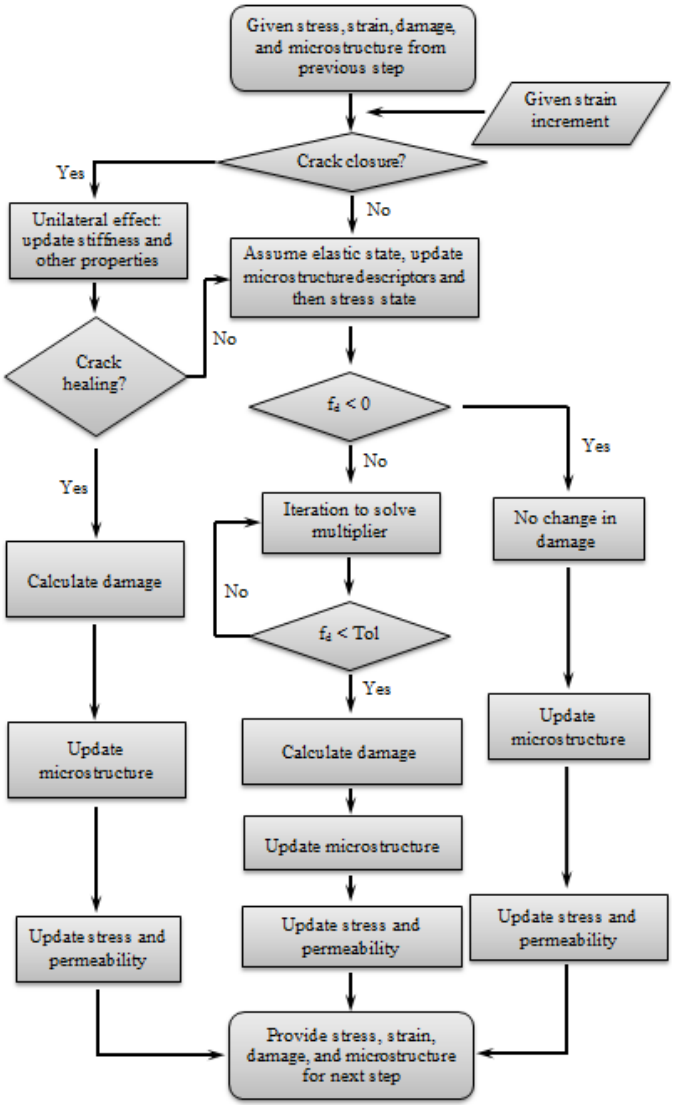

Fig. 9. Computational algorithm of the microstructure-enriched model.

First, the crack closure condition is checked. Crack healing may occur only if crack closure is satisfied. Crack closure influences the stiffness, heat capacity, and bulk modulus, but does not change the microstructure descriptors and damage variable. By contrast, crack geometry evolves during the healing process, which

Table 2. Correlations between microscopic and macroscopic variables

Relation between fabric descriptors and phenomenological variables	
$\boldsymbol{R}$ and $\boldsymbol{A}$	$\boldsymbol{A} = \sum_{j=1}^{3} A_j \boldsymbol{e_j} \otimes \boldsymbol{e_j}$, $A_1 = N_v \frac{r_1^3}{V_{REV}}$, $A_2 = N_v \frac{r_2^3}{V_{REV}}$, $A_3 = N_v \frac{r_3^3}{V_{REV}}$ $\overline{r_j} = \int r_j p_j(r_j) dr_j$
n_{3D} and A_v	$\frac{n_{3D} - n_{3D,lower}}{n_{3D,upper} - n_{3D,lower}} = \frac{n_{2D} - n_{2D,lower}}{n_{2D,upper} - n_{2D,lower}}$ $n_{2D,lower} = \frac{A_{v,lower}}{A_{REV}} = \frac{\pi r^2}{l^2}$, $n_{3D,lower} = \frac{V_{v,lower}}{V_{REV}} = \frac{\frac{4}{3}\pi r^3}{l^3}$ $n_{2D,upper} = \frac{A_{v,upper}}{A_T}$, $n_{3D,upper} = \frac{V_{v,upper}}{V_T}$, $V_{v,upper} = V_T - V_s = A_{tube} \cdot L_{upper} - \frac{m_s}{\rho_s}$ $\overline{n_{2D}} = \int \frac{A_v}{A_{REV}} p_A(A_v) dA$
Relation between fabric descriptor and residual stress	
σ_R and R, A_v	$\sigma_R = N_v \sigma_r = N_v \frac{2\sqrt{2}}{\pi} \frac{\mu}{\kappa + 1} \frac{A_v}{r^2}$

$\overline{r_j}$	=	Mean value of half crack length (m)	A_j	=	Net damage in principal direction j (-)
$n_{2D,lower}$	=	Lower bound of 2D porosity (-)	V_{REV}	=	Volume of REV (m^3)
$n_{3D,lower}$	=	Lower bound of 3D porosity (-)	σ_R	=	Macroscopic residual stress for N_v cracks (Pa)
$n_{2D,upper}$	=	Upper bound of 2D porosity (-)	σ_r	=	Macroscopic residual stress for single crack (Pa)
$n_{3D,upper}$	=	Upper bound of 3D porosity (-)	A_T	=	Longitudinal cross-sectional area of sample cylinder (m^2)
V_s	=	Volume of the salt solid (m^3)	V_T	=	Total volume of the sample cylinder (m^3)
ρ_s	=	Density of the salt solid (kg/m^3)	A_v	=	Void area (m^2)
m_s	=	Mass of the salt solid (kg)	A_{tube}	=	Inner cross-sectional area of tube (m^2)

results in a change in mixed damage variable and stress state.

If crack closure does not occur, we use the damage criterion to determine whether the material reaches its damage state or remains elastic during the current increment. In the elastic domain (elastic loading or unloading), the damage in the material does not change and only the microstructure changes, which induces a change in stress. If damage occurs, iterations are required to update the new damage variable. The microstructure and stress variables will be updated accordingly.

Based on the calculation at the current step, strain, stress, damage, and microstructure variables are updated and stored for the next computational step.

5. NUMERICAL SIMULATION

We simulate a strain-controlled uniaxial loading test in MATLAB. The stress path consists of uniaxial tension, tension unloading, healing, and reloading in tension. We assume that only the healing phase is time-dependent. Mechanical loads are applied instantaneously. Table 3 provides the model parameters used in the simulations, after (Zhu and Arson, 2014; Zhu and Arson, 2015a). Mechanical loading and unloading phases was assumed to take place at room temperature (22°C = 295K), whereas the healing process was simulated at elevated temperatures (595K, 695K). The healing period was 10,000s (about 2.8 hours).

Table 3. Model parameters used for the strain-controlled uniaxial test (compression counted positive).

λ (Pa)	μ (Pa)	α (Pa)	β (Pa)
2.63e10	1.75e10	1.9e9	-2.04e10
g (Pa)	C_0 (Pa)	C_1 (Pa)	α_T (K^{-1})
1.1e8	200	1e5	-1e-5
U_0 (-)	l (m)	e_0 (-)	t (-)
1	1e-4	0.008	-1.2
$n_{2D,lower}$ (-)	$n_{2D,upper}$ (-)	$n_{3D,lower}$ (-)	$n_{3D,upper}$ (-)
0.03	0.165	0.004	0.321
R_{min} (m)	R_{max} (m)	A_{min} (m^2)	A_{max} (m^2)
1e-4	1e-3	1e-12	1e-10

The stress-strain response follows the expected trends (Fig. 10a). The linear segment (OA) represents the initial elastic response - until damage initiates at point A. The accumulation of damage degrades the stiffness (AB) before the unloading phase. After releasing all tensile stress (BC) and applying additional compression to close all cracks (CD), unilateral effects result in some unilateral recovery of the stiffness in compression (DE). Healing occurs at elevated temperature (EF). Temperature was set back to room temperature before initiating tensile deformation for the reloading phase (FG). Additional damage is produced after recovery (GH) when the new damage threshold is reached. The change in slope after reloading illustrates the effect of

temperature on healing: higher temperature over the same period of time leads to a more mechanical recovery (i.e., stiffness recovery).

The evolution of damage is the same for both healing temperatures investigated (Fig. 10b). Micro-cracks do not propagate during the elastic phase (OA) or the unloading phase (BCDE). Damage increases during the non-elastic tension phase (AB), remains constant during healing phase (EF), and increases again during reloading (GH). The mixed damage variable evolution follows a similar trend except during the healing phase (Fig. 10c). When healing occurs at constant axial deformation, *h* increases due to crack rebonding, which results in a decrease in A_1. After 10,000s' healing at 595K and 695K, the healed stiffness increases from 81% of the initial stiffness (after damage and before healing, point E) to 86% and 89% of the initial stiffness (after healing, point F), respectively. Comparing with healing processes that occur in the presence of brine (Zhu and Arson, 2015b), healing in dry conditions is relatively slower and requires higher temperature or longer healing time to produce the same effect.

Evolutions of fabric descriptors are presented in Fig. 10d and Fig. 10e. Because of the axis-symmetry of the problem and by construction of the model, micro-cracks only propagate in planes orthogonal to the loading direction ($R_2 = R_3 \neq 0$, $R_1 = 0$). Since crack length is updated with net damage, evolution of crack length is similar to that of net damage (Fig. 10d). Crack aperture increases during elastic phase and decreases when damage propagates (Fig. 10e), which means that micro-cracks become longer but thinner during crack propagation.

The material permeability depends on the evolution of microstructure descriptors (Eq. 12 and 13). The overall trend of permeability evolution is similar to the evolution of the crack radius (Fig. 10f). Permeability increases slightly during the elastic phase since the crack aperture increases (OA). Note that we assumed that salt had a non-zero initial permeability. Therefore, the variations of permeability due to damage shown in Fig.7 occur in addition to that initial permeability in our simulation results. When damage starts to accumulate after point A, the radius of cracks increases, which rapidly leads to the percolation threshold (Fig. 7 in Section 3.3). That is why permeability increases dramatically after the initiation of damage (AB). Once the crack network stabilizes and forms a fully connected flow path, the permeability will gradually reach its maximum value. Similar trends were observed in many experimental studies (e.g., Alkan, 2009). During unloading, crack aperture decreases, however, crack faces are not fully rebonded. As a result, permeability decreases but does not go back to its initial value (BCDE). The change of crack radius also contributes to the decrease of permeability during healing (EF). Crack radius and permeability increase again when the new damage criterion is satisfied during reloading (GH).

Permeability evolution is governed by changes of porosity (or equivalently REV volume since grains are incompressible, Fig. 10h) and pore connectivity (Fig. 10g). It is obvious that connectivity varies significantly when damage or healing occurs, whereas the REV volume change is negligible. Therefore, permeability evolution is controlled by crack connectivity for the case simulated.

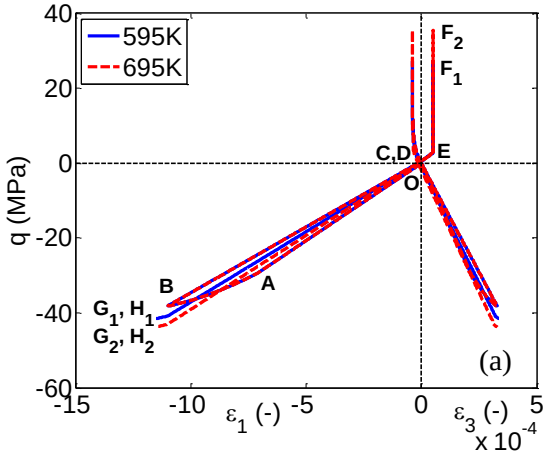

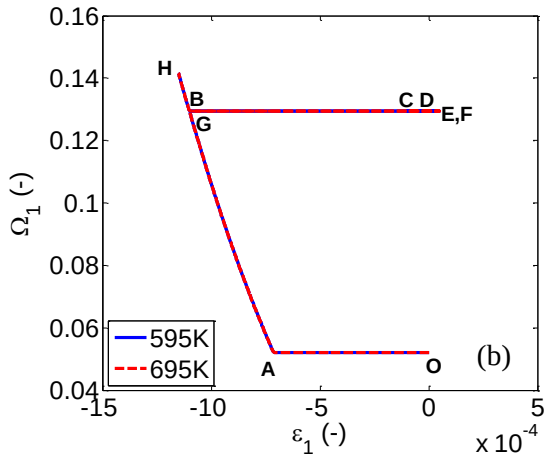

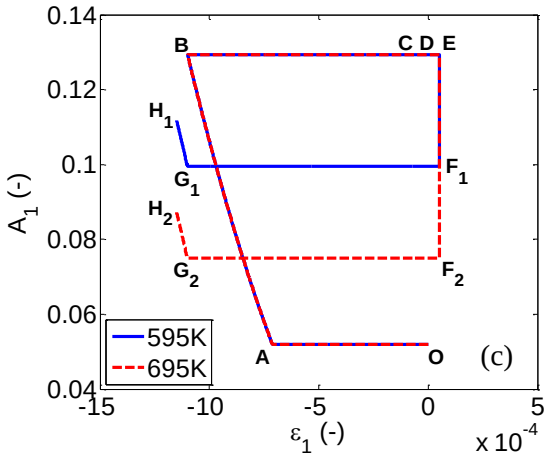

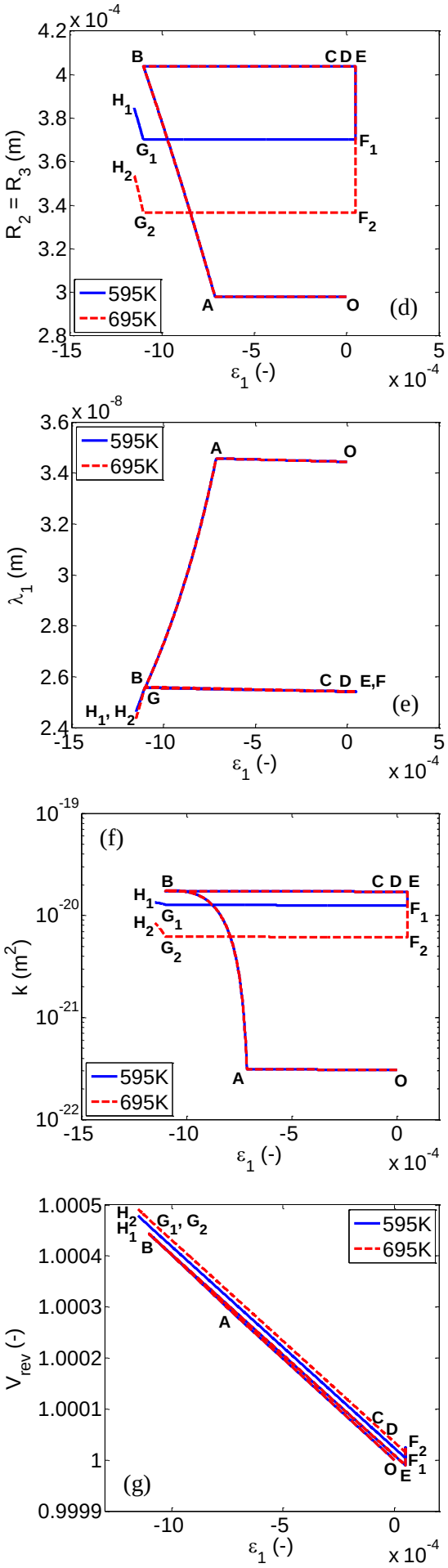

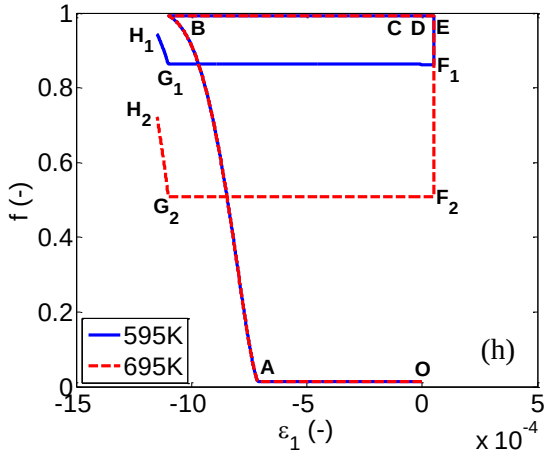

Fig. 10. Numerical simulation results from MATLAB at the integration point: (a) stress-strain; (b) damage variable; (c) net damage variable; (d) crack radius; (e) crack aperture; (f) permeability; (g) volume change; (h) connectivity.

6. CONCLUSION

In this study, we formulate a Continuum Damage Mechanics model that couples the evolution of salt microstructure with the changes of stiffness, deformation, and permeability upon mechanical damage and chemical healing. The free energy is expressed as a polynomial consisting of a purely thermo-elastic potential and a damaged energy component. We introduce a unilateral condition in the expression of stiffness to account for the effects of crack closure. Diffusive Mass Transfer (DMT) is assumed to dominate the healing processes that lead to rebonding. Deformation, stress, and permeability are coupled to salt fabric descriptors including crack area, length, aperture, and spacing. We characterized the probability density function of these descriptors by statistical image analysis. Images were acquired with microscopes and micro-CT scans at regular time intervals during creep tests performed on table salt.

We designed a MATLAB resolution algorithm at the integration point in order to predict iteratively the variations of microstructure variables and macroscopic phenomenological variables during a test comprising a tensile loading phase, a compressive unloading phase, a creep-healing phase, and a reloading phase. Healing was simulated at two different elevated temperatures. Results highlight the increased efficiency of healing with temperature and illustrate the coupling between microstructure evolution and variations of mechanical properties. Simulations also show that permeability changes are controlled by changes in crack connectivity, which dominate changes of porosity.

In order to improve the predictions of stiffness, deformation and fabric, proper calibration with more experimental data is necessary. In addition to rigorous

calibration, our future work will focus on the reconstruction of the pore network based on 3D image processing to estimate the flow anisotropy. The proposed modeling approach is expected to improve the fundamental understanding of damage and healing in rocks at both macroscopic and microscopic scales, and to better predict the long-term behavior of geological storage facilities.

ACKNOWLEDGEMENTS

Financial support for this research was provided by the National Science Foundation (Grant No. CMMI-1362004/1361996).

REFERENCES

1. Abramoff, M. D., P. J. Magalhaes, and S. J. Ram. 2004. Image processing with ImageJ. *Biophotonics international.* 11 (7): 36–42.
2. Alkan, H. 2009. Percolation model for dilatancy-induced permeability of the excavation damaged zone in rock salt. International Journal of Rock Mechanics and Mining Sciences. 46: 716-724.
3. Anderson, T. 2005. *Fracture Mechanics: Fundamentals and Applications.* 3rd Edition. Taylor & Francis.
4. Chaboche, J. L. 1992. Damage induced anisotropy: on the difficulties associated with the active/passive unilateral condition. *Int. J. Damage. Mech*. 1 (2): 148-171.
5. Chan, K. S., S. R. Bodner, and D. E. Munson. 2001. Permeability of WIPP salt during damage evolution and healing. International Journal of Damage Mechanics. 10: 347-375.
6. De Gennes, P. G. 1976. *The physics of liquid crystals*. Oxford University Press, Oxford.
7. Dienes, J. K. 1982. Permeability, percolation and statistical crack mechanics. In: R. E. Goodman and F. E. Heuze (Editors). *Metallurgical and Petroleum Engineering*. New York, pp. 86-94.
8. Gloyna, E. F. and T. D. Reynolds. 1961. Permeability measurements of rock salt. *Journal of geophysical research*. 66 (11): 3913-3921.
9. Guéguen, Y. and J. Dienes. 1989. Transport properties of rocks from statistics and percolation. *Mathematical Geology*. 21 (1): 1-13.
10. Hou, Z.M. 2003. Mechanical and hydraulic behavior of rock slat in the excavation disturbed zone around underground facilities. *International Journal of Rock Mechanics and Mining Sciences*. 40(5): 725-738.
11. Mapother, D., H. N. Crooks, and R. Maurer. 1950. Self-diffusion of sodium in sodium chloride and sodium bromide. *The Journal of Chemical Physics.* 18:1231-1236.
12. Oda, M., T. Takemura, and T. Aoki. 2002. Damage growth and permeability change in triaxial compression tests of Inada Granite. *Mechanics of Materials*. 34: 313-331.
13. Peach C. J. 1990. Influence of deformation on the fluid transport properties of rock salts. PhD dissertation, Instituut voor Aardwetenschappen der Rijksuniversiteit, Utrecht, Holland.
14. Peach, C. J. and C. J. Spiers. 1996. Influence of crystal plastic deformation on dilatancy and permeability development in synthetic salt rock. *Tectonophysics*. 256: 101-128.
15. Shen, X., C. Zhu and C. Arson. 2016 (under review). Chemo-mechanical damage and healing of granular salt: micro-macro modeling, *50th Rock Mechanics and Geomechanics Symposium*. June 26-29 2016. Houston, Texas, USA.
16. Stauffer, D. 1985. *Introduction to percolation theory*. Taylor and Francis, London.
17. Zhu, C. and C. Arson. 2014. A thermo-mechanical damage model for rock stiffness during anisotropic crack opening and closure. *Acta Geotechnica*. 9 (5): 847-867.
18. Zhu, C. and C. Arson. 2015a. A model of damage and healing coupling halite thermos-mechanical behavior to microstructure evolution. *Geotechnical and Geological Engineering*. 33 (2): 389-410.
19. Zhu, C. and C. Arson. 2015b. Fabric-enriched modeling of anisotropic healing induced by diffusion in granular salt. *The 49th US Rock Mechanics / Geomechanics Symposium.* 28 June – 1 July 2015. San Francisco, CA, USA.